A Final Report
NASA Grant No. NAG3-1334

HIGH PERFORMANCE MAGNETIC BEARINGS
FOR AERO APPLICATIONS

Submitted to:

Submitted by:

P. E. Allaire, Wade Professor

C. R. Knospe, Assistant Professor

R. D. Williams, Associate Professor

D. W. Lewis, Professor

L. E. Barrett, Professor

E. H. Maslen, Associate Professor

R. R. Humphris, Professor Emeritus

SEAS Report No. UVA/528425/MANE97/101
February 1997

**DEPARTMENT OF MECHANICAL, AEROSPACE AND
NUCLEAR ENGINEERING**

SCHOOL OF
ENGINEERING
& APPLIED SCIENCE

University of Virginia
Thornton Hall
Charlottesville, VA 22903

HIGH PERFORMANCE MAGNETIC BEARINGS FOR AERO APPLICATIONS

FINAL REPORT

Submitted To:

National Aeronautical and Space Administration
Lewis Research Center
Mail Stop 500-309
21000 Brookpark Road

Attention:

Ms. Kaprice Harris
Grants Officer
Tel: 216-433-2457

For Consideration By:

Mr. Andrew Provenza
Project Monitor
Tel: 216-433-6047

Submitted By:

P. E. Allaire, Wade Professor
(Tel: 804-924-6209/e-mail: pea@virginia.edu)
C. R. Knospe, Assistant Professor
R. D. Williams, Associate Professor
D. W. Lewis, Professor
L. E. Barrett, Professor
E. H. Maslen, Associate Professor
R. R. Humphris, Professor Emeritus

Mechanical, Aerospace and Nuclear Engineering
University of Virginia
Charlottesville, VA 22901

February 5, 1997

SECTION 1

INTRODUCTION

1.1 PREVIOUS AND FINAL WORK

Several previous annual reports were written and numerous papers published on the topics for this grant. That work is not repeated here in this final report. Only the work completed in the final year of the grant is presented in this final report. This final year effort concentrated on power loss measurements in magnetic bearing rotors.

1.2 SIGNIFICANCE

The effect of rotor power losses in magnetic bearings are very important for many applications. In some cases, these losses must be minimized to maximize the length of time the rotating machine can operate on a fixed energy or power supply. Examples include aircraft gas turbine engines, space devices, or energy storage flywheels. In other applications, the heating caused by the magnetic bearing must be removed. Excessive heating can be a significant problem in machines as diverse as large compressors, electric motors, textile spindles, and artificial heart pumps.

1.3 BEARING GEOMETRY CONFIGURATIONS

There are two primary different magnetic bearing configurations that are employed in industrial applications: heteropolar and homopolar. There are many conflicting claims made with regard to which is the lower power loss bearing but there is little experimental data in the literature on this topic. Also, there is currently no effective way of calculating the power losses with a computer code such as a finite element modeling approach. There are a number of industrial firms which manufacture each type.

Figure 1.1 shows a heteropolar design configuration. The magnetic flux paths are essentially planar (in the plane perpendicular to the axis of rotation) with half of the poles North and the other half of the poles South. Thus the poles are different as one traverses the bearing in the circumferential direction, leading to the name "heteropolar".

A homopolar bearing configuration is shown in Figure 1.2. It has a full three dimensional magnetic flux path but a significant portion of the magnetic flux path is axial in nature.

Radial (Heteropolar)
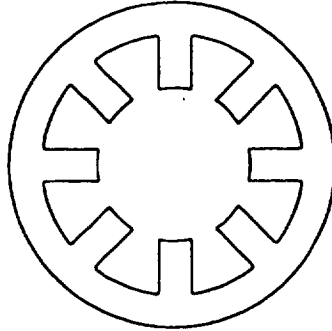
8 pole

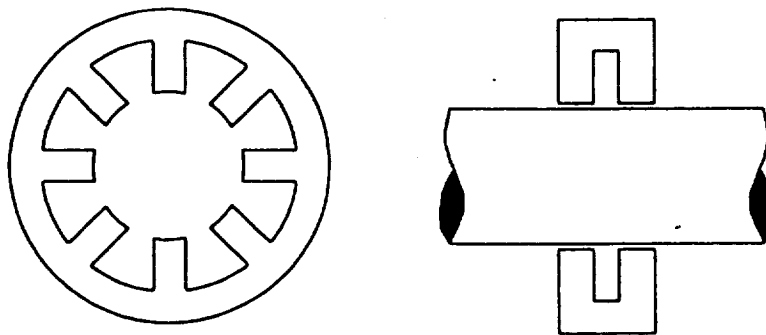**Figure 1.1 Heteropolar Magnetic Bearing Configuration**

Radial (Homopolar)

Figure 1.2 Homopolar Magnetic Bearing Configuration

Page 1.3

In a given plane (perpendicular to the axis of rotation), the poles are all either North or South. This uniformity in regard to the type of pole in one plane has lead to the name "homopolar" for this bearings type.

EXPERIMENTAL LITERATURE REVIEW

Power loss studies in magnetic bearings published in the open literature have been very limited. Matsumura, et al [1] discussed magnetic bearing losses including a partial Fourier analysis of magnetic flux as seen by the rotor as it passes the poles in the bearing. Higuchi, et al. [2] presented some experimental rotating loss data in magnetic bearings. Ueyama and Fujimoto [3] gave power loss results for an eight pole radial bearing. Matsumura and Hatake [5] discussed a Fourier analysis of fringing and leakage effects on eddy current losses, indicating that pole edge effects may be the most important consideration. Kasarda et al. [5,6] conducted loss measurements in a low speed test rig, operating up to approximately 2800 rpm (DN = 175,000), in air.

Kasarda, et al. [7] discussed the design of the present high speed test rig in some detail and gave a sensitivity analysis of the loss modeling based upon the theoretical parameters involved. Kasarda, et al. [8] presented high speed loss results, using the same test rig employed for the work in this paper, for an 8 pole radial bearing constructed of silicon iron laminated materials. The rotor operated at a top speed of about 32,000 rpm, corresponding to a DN value of 2.9×10^6 mm rpm. Variations in pole winding configuration and bias flux were examined. Bias flux was found to be very significant while pole winding was found to be not very significant. An analytical /empirical model was then applied to the loss measurements by Kasarda, et al. [9].

FINITE ELEMENT LITERATURE REVIEW

Finite element magnetic field calculations have been discussed in the literature for some time. Sarma [11] derived a magnetic vector potential (A) and an electric vector potential (ϕ) for non-linear, time dependent electromagnetic field problems but did not consider motion of the magnetic material. Muramatsu et al. [12] considered a set of coupled vector differential equations for A and ϕ in fixed and moving coordinate systems for eddy current analysis in moving conductors.

Chan and Williamson [13] considered the analysis of eddy current problems involving relative motion. They also obtained a coupled differential equation for A and ϕ in three dimensions. Ito et al. [14] developed a time dependent differential equation for A including traveling magnetic field effects (motional effects) which is uncoupled from ϕ but involves the curl of the magnetic vector potential.

Allaire et al. [15] presents a general three dimensional formulation of the uncoupled magnetic and electric field equations for magnetic bearing configurations. A Galerkin weighted residual method [16] is employed to evaluate the element matrices.

High velocities in the magnetic material can introduce numerical instabilities in some solutions. A method of upwinding is required to remove the instability. Several methods have been proposed in the literature [13,14,17,18]. In this paper, upwinding is implemented using the technique developed by Heinrich and Yu [19] and Pepper and Heinrich [20]. This method employs an expanded form of the Galerkin weighting function, sometimes called a Petrov-Galerkin weighting function.

Rockwell et al. [21] and Rockwell [23] presented an uncoupled formulation of the magnetic vector potential starting with Maxwell's equations. The method of weighted residuals was employed to develop the element matrices for a two dimensional analysis and upwinding was used to eliminate numerical instability. This finite element approach was applied to an example radial magnetic 8 pole bearing with one pair of poles activated. It was found that numerical instabilities had only minor effects when a full 360 degree bearing model was solved. Meeker and Maslen [22] presented a boundary element model using a thin plate model of a bearing lamination for evaluating power losses. Power losses were obtained for one bearing configuration and compared to eddy current power losses derived from measured values with good results.

Rockwell et al. [24] starts with Maxwell's equations and develops an uncoupled form of the governing differential equation for the magnetic vector potential. The eddy currents are then and associated rotor power losses are evaluated separately [25]. Only two dimensional equations are treated [24,25].

SECTION 2

EXPERIMENTAL MEASUREMENTS

2.1 TEST RIG

An advanced, dedicated power loss test rig was developed under previous NASA Lewis Research Center funding, under Grant No. NAG3-1334. The test rig consists of a shaft with two magnetic bearings and two induction motors located at the shaft ends, as shown in Fig. 2.1. It has been designed to measure the power losses in magnetic bearings by accurately measuring the conversion of the rotor's kinetic energy into heat.

The test rig has been designed so that the only significant loss mechanisms come from the magnetic bearings: eddy current losses, hysteresis losses, and air drag. The two electric motors drive the rotor up to peak operating speed and then they are shut off. The motor stators have been shown to not have any significant residual magnetic drag during run down [8].

A vacuum chamber will be employed in this project work to eliminate air drag but that feature was not in place for the work reported here. No thrust bearings are present in the test rig: the rotor is centered by reluctance forces in the radial bearings. Thus there are no thrust bearing losses.

Fig. 2.2 shows a rotor assembly drawing. The outer diameter of the bearing journals is approximately 89.0 mm (3.5 in) and the test rig is designed to operate up to 50,000 rpm resulting in a DN of 4.5×10^6 mm-rpm. However, the yield strength of the current silicon iron bearing limits the peak speed to 32,000 rpm. The rotor first critical speed is at approximately 84,000 rpm so the rotor is considered rigid. Fig. 2.3 shows a full assembly drawing of the test rig. Additional details of the test rig design are given in [7].

2.2 DATA REDUCTION

This is done by measuring the time it takes for the rotor to run down from one speed to another. The rotor kinetic energy due to rotation is
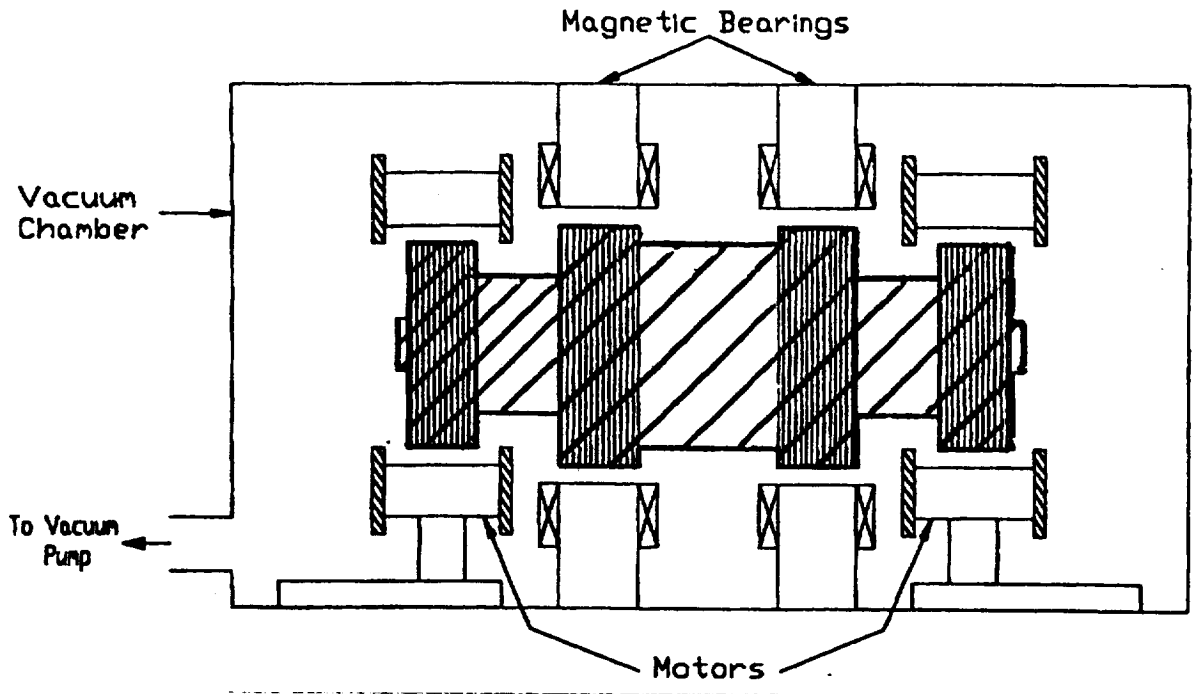
$$E_k = \frac{1}{2}J\omega^2 \tag{1}$$
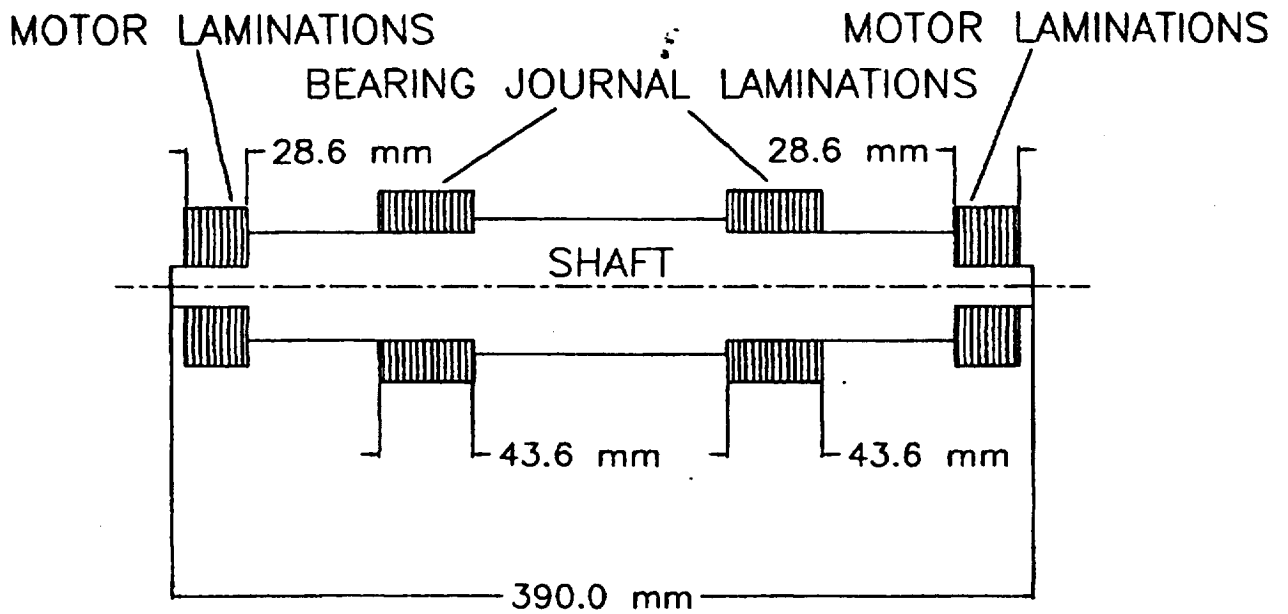
Figure 2.1. Diagram of Magnetic Bearing Loss Test Rig
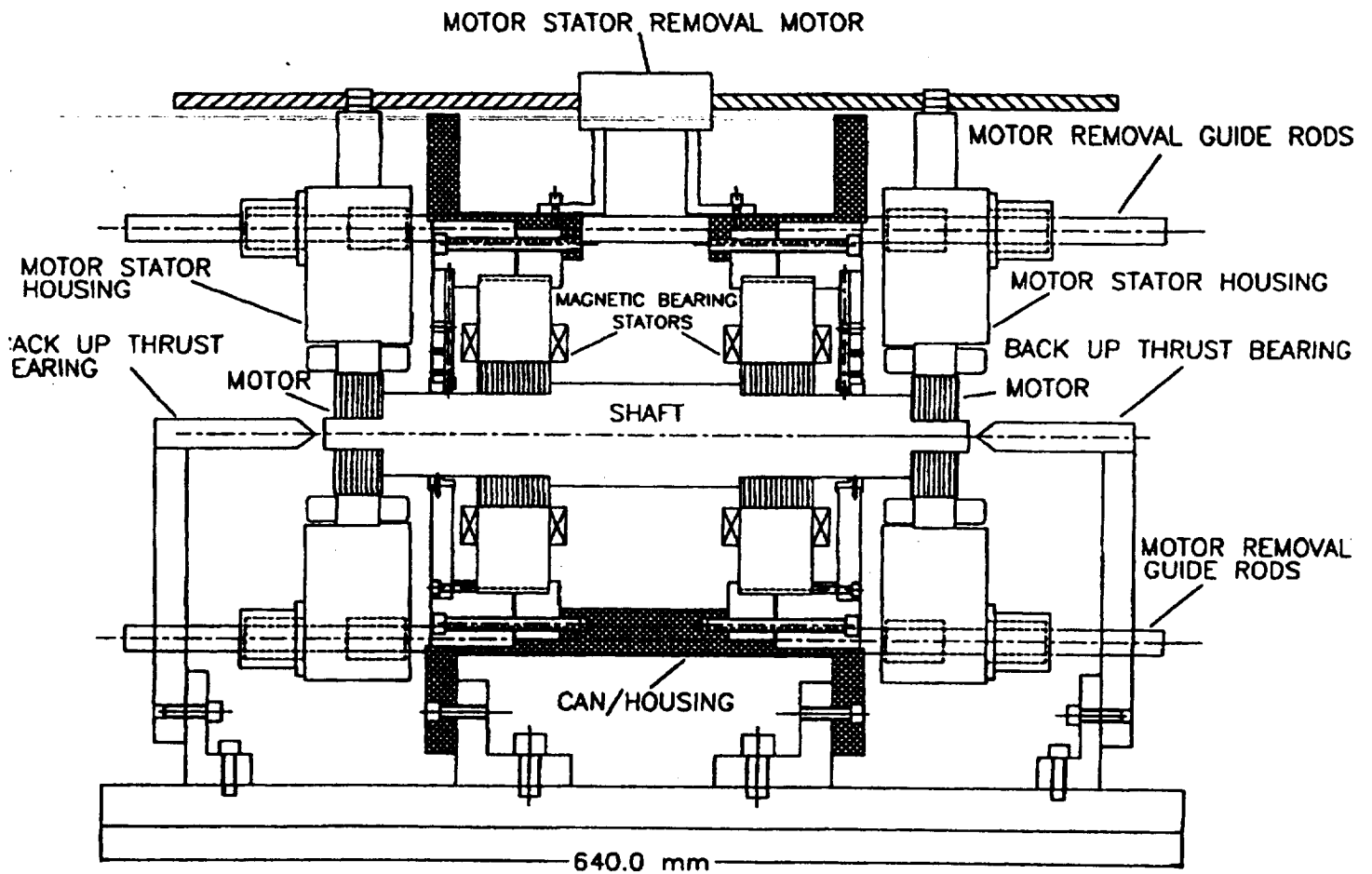

Figure 2.2. Rotor Assembly Drawing

MOTOR STATOR REMOVAL MOTOR

MOTOR REMOVAL GUIDE RODS

MOTOR STATOR
HOUSING

MAGNETIC BEARING
STATORS

MOTOR STATOR HOUSING

ACK UP THRUST
EARING

BACK UP THRUST BEARING

MOTOR

MOTOR

SHAFT

MOTOR REMOVAL
GUIDE RODS

CAN/HOUSING

640.0 mm

Figure 2.3. Full Test Rig Assembly Drawing

Page 2.3

where ω is the rotational speed in rad/s. The power loss is the time derivative of the kinetic energy

$$P_k = \frac{dE_k}{dt} = J\omega\frac{d\omega}{dt} + \frac{\omega^2}{2}\frac{dJ}{dt} \qquad (2)$$

The second term is small for this test because the rotor does not have large dimensional changes so this expression reduces to

$$P_k = J\omega\frac{d\omega}{dt} = \left(\frac{\pi}{30}\right)^2 JN\frac{dN}{dt} = P_h + P_e + P_v \qquad (3)$$

where P_k=Power Loss (watts), J=Polar Moment of Inertia (N-s^2-m), and dN/dt=Deceleration Rate (rpm/s). The polar moment of inertia of the rotor, J, is easily determined from a calculation and N(t) is easily measured from the rundown tests. On the right hand side of this equation, the power loss is written as the sum of the power loss due to hysteresis, P_h, the power loss due to eddy currents, P_e, and the power loss due to windage, P_w.

It has been shown in previous work [7,8,9] that the power loss can be written in terms of frequency dependent parameters as

$$P_k = C_h\omega + C_e\omega^2 + C_v\omega^{2.8} \qquad (4)$$

based upon analytical/empirical models. In this formula, the skin effects are neglected [8]. Analytical/empirical modeling results including skin effects for the data presented in this paper are not available at this time.

The measured data was recorded as speed (in rpm) vs. time (in seconds). The rundown data dN/dt was evaluated using the following model

$$\frac{dN}{dt} = b_1 + b_2N + b_3N^{1.8} \qquad (5)$$

where the coefficients are defined as

$$b_1 = \frac{C_h}{J(\pi/30)^2} \ ; \ b_2 = \frac{C_e}{J(\pi/30)^2} \ ; \ b_3 = \frac{C_v}{J(\pi/30)^2} \qquad (6)$$

from (3) and (4). An analytical expression for the actual speed curve was determined for each case and minimized using a simplex search method [8]. The calculated power loss components were then determined from (4) and (6).

2.3 HETEROPOLAR BEARING PREVIOUS RESULTS

The radial bearing geometry is shown in Fig. 2.4. Six measured power loss curves are given in Fig. 2.5. They cover: bearing No. 1 (rotor R1 with air gap of 0.762 mm (0.030 in)) for static flux levels of 0.4, 0.5 and 0.6 tesla and bearing No. 2 (rotor R2 with air gap of 0.381 mm (0.015 in)) for static flux levels of 0.4, 0.5 and 0.6 tesla vs. rotational speed from 0 to 28,000 rpm. Table No. 2.1 gives example measured loss values at 28,000 rpm.

Table 2.1. Example Measured Rotor Power Loss vs. Bias Current and Nomial Bias Flux Density For Two Air-Gap Thicknesses at 28,000 rpm.

	Bearing No. 1 (Gap = 0.762 mm)	Bearing No. 2 (Gap = 0.381 mm)
B = 0.4 Tesla	580 watts	929 watts
B = 0.5 Tesla	683 watts	1385 watts
B = 0.6 Tesla	795 watts	1497 watts

The coefficients b_1, b_2 and b_3 are given in Table 2.2 for the data in Fig. 2.5 with the air gap of 0.76 mm (0.030 in). The effect of various mechanisms for power loss are indicated by the coefficients in Table 2.2 and the specific loss values for each component are given in Table 2.3.

An important effect is the air gap thickness. The rotor power loss increases for smaller air gaps but evaluating the specific the numerical value is critical. Table 2.4 gives the corresponding coefficients for the bearing with air gap of 0.38 mm (0.015 in) and Table 2.5 gives specific values at 28,000 rpm.

The hysteresis coefficients are nearly the same for both bearings at a given value of flux density indicating that the hysteresis effects are nearly the same for each bearing. The eddy current coefficients are much larger, by a factor of 2 to 3, for the case with the smaller gap of 0.381 mm (0.015 in). Thus the eddy currents are the major difference in the larger losses at lower gap thickness.

Radial (Heteropolar)
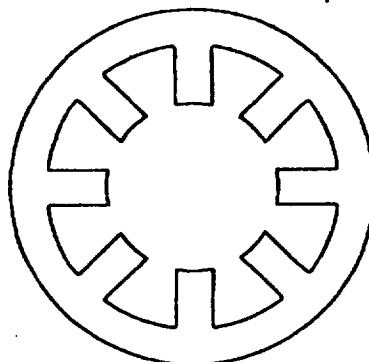
8 pole

Figure 2.4. Radial Bearing Geometry

Table 2.2. Power Loss Coefficients For Magnetic Bearing No. 1
Data Presented in Fig. 2.5 For Three Bias Flux Density Values and
Air Gap Thickness 0.76 mm (0.030 in).

	Flux Density (B) = 0.4 T	Flux Density (B) = 0.5 T	Flux Density (B) = 0.6 T
Hysteresis Coefficient (rpm/s)	$b_1=-17.6$	$b_1=-22.1$	$b_1=-26.8$
Eddy Current Coefficient (1/s)	$b_2=-4.6 \times 10^{-3}$	$b_2=-6.2 \times 10^{-3}$	$b_2=-7.9 \times 10^{-3}$
Windage Coefficient ($1/\text{rpm}^{0.8}\text{s}$)	$b_3=-8.6 \times 10^{-7}$	$b_3=-7.8 \times 10^{-7}$	$b_3=-7.1 \times 10^{-7}$

Table 2.3. Calculated Power Loss Components in Magnetic Bearing
No. 1 with Three Bias Flux Values and Air Gap Thickness 0.76 mm
(0.030 in) at 28,000 rpm.

	Flux Density (B) = 0.4 T	Flux Density (B) = 0.5 T	Flux Density (B) = 0.6 T
Hysteresis Loss (watts)	44	55	67
Eddy Current Loss (watts)	320	432	550
Windage Loss (watts)	216	196	179

The windage coefficients are nearly the same for the two
bearings when the bias flux density is the same. There is a
difference in the bias flux density of 0.6 tesla for the small
gap configuration which is not well explained at this time.

2.5 STATIC MAGNETIC FLUX DENSITY MEASUREMENTS

The static magnetic flux density was measured in the air
gaps for all cases to serve as an independent check on the
magnetic flux density in the air gaps. A Hall probe of thickness
0.254 mm (0.010 in) was inserted into each of the eight air gaps
in the bearing and the measured flux noted and found to be nearly
constant in the air gap. The shaft was not rotating during the
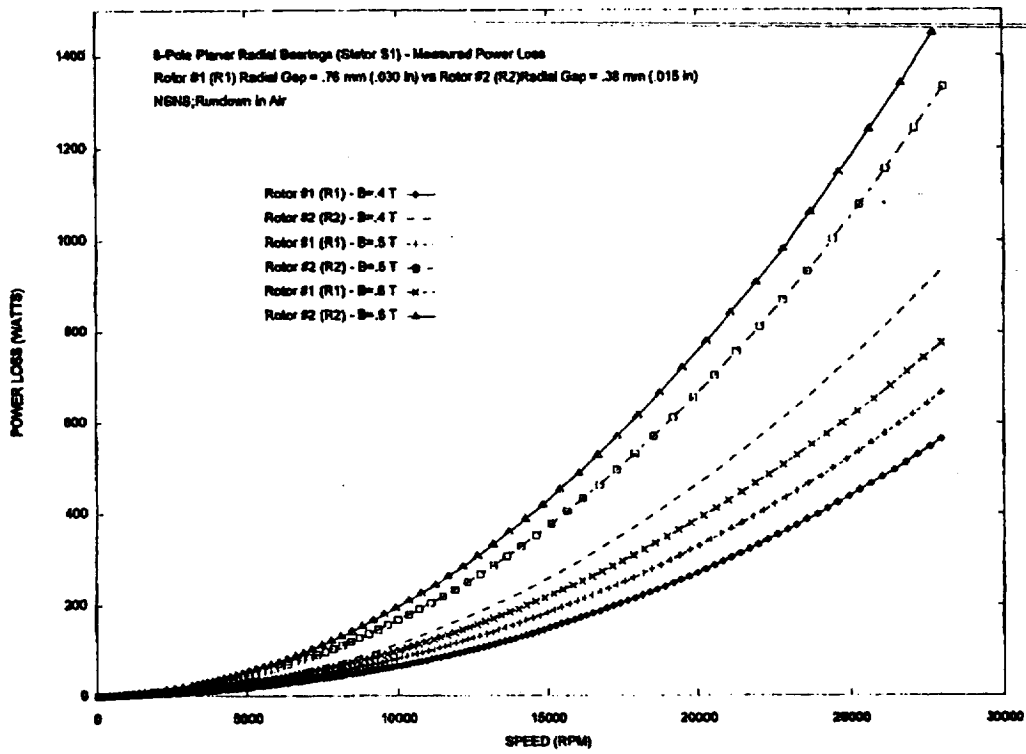measurements.

NASA Highspeed Power Loss Test Rig

Figure 2.5. Measured Bearing Power Loss Values

Table 2.4. Power Loss Coefficients For Magnetic Bearing No. 2 Data Presented in Fig. 2.5 For Three Bias Flux Density Values and Air Gap Thickness 0.38 mm (0.015 in).

	Flux Density (B) = 0.4 T	Flux Density (B) = 0.5 T	Flux Density (B) = 0.6 T
Hysteresis Coefficient (rpm/s)	$b_1 = -16.0$	$b_1 = -22.2$	$b_1 = -25.2$
Eddy Current Coefficient (1/s)	$b_2 = -1.0 \times 10^{-2}$	$b_2 = -1.6 \times 10^{-2}$	$b_2 = -1.9 \times 10^{-2}$
Windage Coefficient $(1/rpm^{0.8}s)$	$b_3 = -7.4 \times 10^{-7}$	$b_3 = -8.2 \times 10^{-7}$	$b_3 = -4.0 \times 10^{-7}$

Table 2.5. Calculated Power Loss Components in Magnetic Bearing No. 2 with Three Bias Flux Values and Air Gap Thickness 0.38 mm (0.015 in) at 28,000 rpm.

	Flux Density (B) = 0.4 T	Flux Density (B) = 0.5 T	Flux Density (B) = 0.6 T
Hysteresis Loss (watts)	40	56	63
Eddy Current Loss (watts)	701	1122	1333
Windage Loss (watts)	187	208	101

Example measured static bias flux values are given in Table 2.6 for a nominal bias flux density of 0.6 tesla. The bias current in the bearing coils corresponding to the data in Table 2.6 was 3.50 A for bearing No. 1 and 1.94 A for bearing No. 2. The difference in the air gaps is due to the load on the bearing and experimental variability on using the flux probe. The average value for both bearings is approximately 0.62 tesla.

HOMOPOLAR BEARING PREVIOUS RESULTS

A 2-plane, 8 pole homopolar bearing was tested. Figure 6 shows the geometry of the bearing. The stator, S2, was constructed of 0.356 mm (0.014 in) 3% silicon iron laminations. The rotor, R3, has 3% silicon iron laminations thickness of 0.356

Table 2.6. Measured Static Air Gap Flux Levels in Bearings No. 1 and No. 2.

Pole No.	Stator No.1 Magnetic Flux Density (T)	Stator No. 2 Magnetic Flux Density (T)
1	0.71	0.68
2	0.60	0.62
3	0.66	0.66
4	0.59	0.57
5	0.62	0.63
6	0.56	0.52
7	0.67	0.70
8	0.56	0.59

mm (0.014 in). The air gap thickness was 0.381 mm (0.015 in) for the homopolar bearing.

Rundown data was taken for the homopolar bearing operating in the same speed range as the heteropolar bearing. Figure 2.6 shows a plot of the rundown data for both the heteropolar bearing No. 2 and the homopolar bearing No. 3 at a bias flux density of 0.3 Tesla. The speed range is up to 30,000 rpm. The air gap thickness and flux density is the same for both bearings so the curves clearly indicates the lower loss performance of the homopolar design.

This data was converted to power loss data and the results plotted in Fig. 2.7. The power loss values were converted into loss coefficients as indicated above. The hysteresis coefficient, b_1, is lower for the homopolar bearing. This is to be expected as rotating hysteresis losses should be lower in the homopolar bearing. The eddy current coefficient, b_2, is also significantly lower. The windage coefficient is approximately the same indicating that the longer length rotor does not apparently develop much higher windage loss.
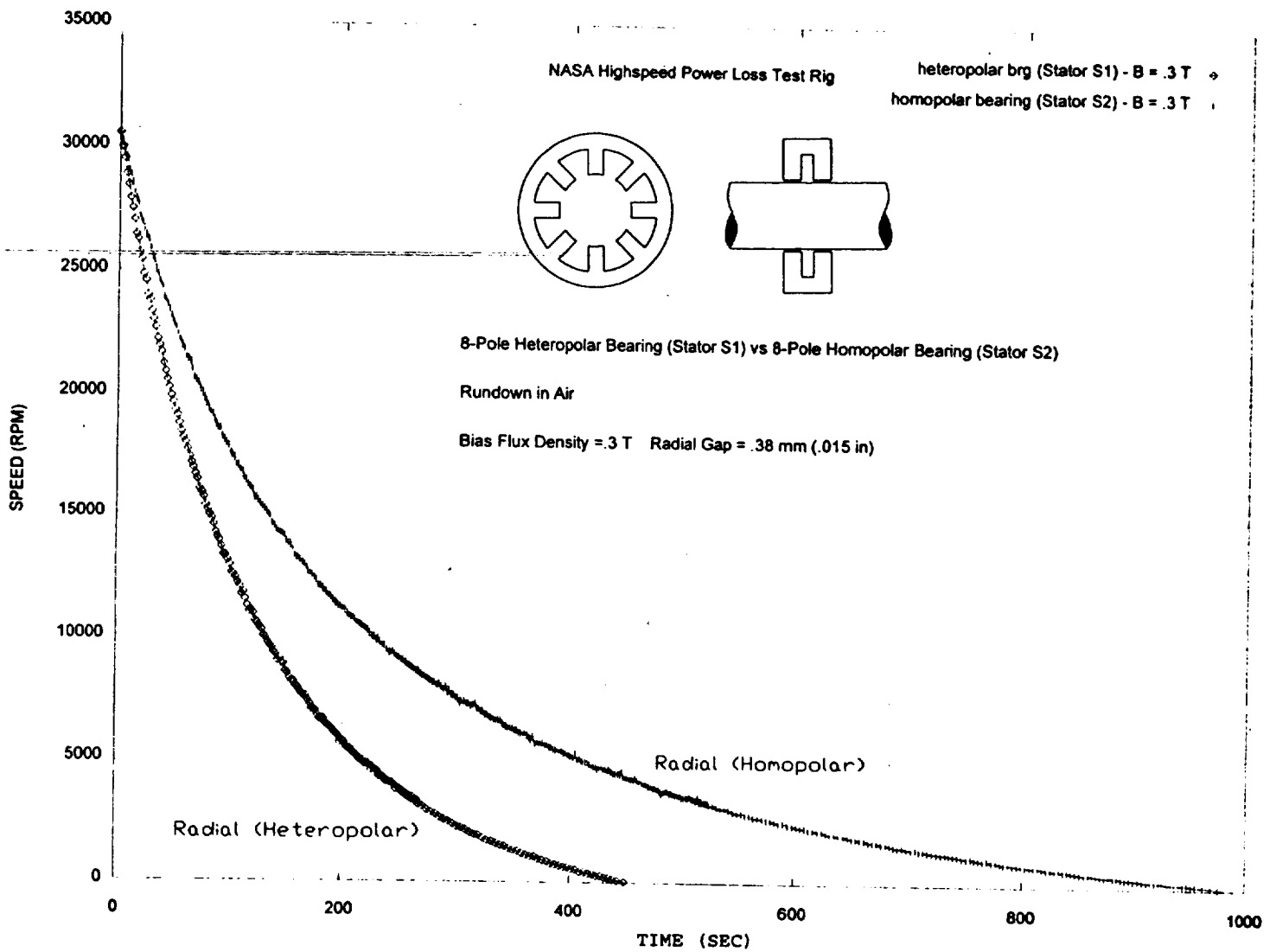
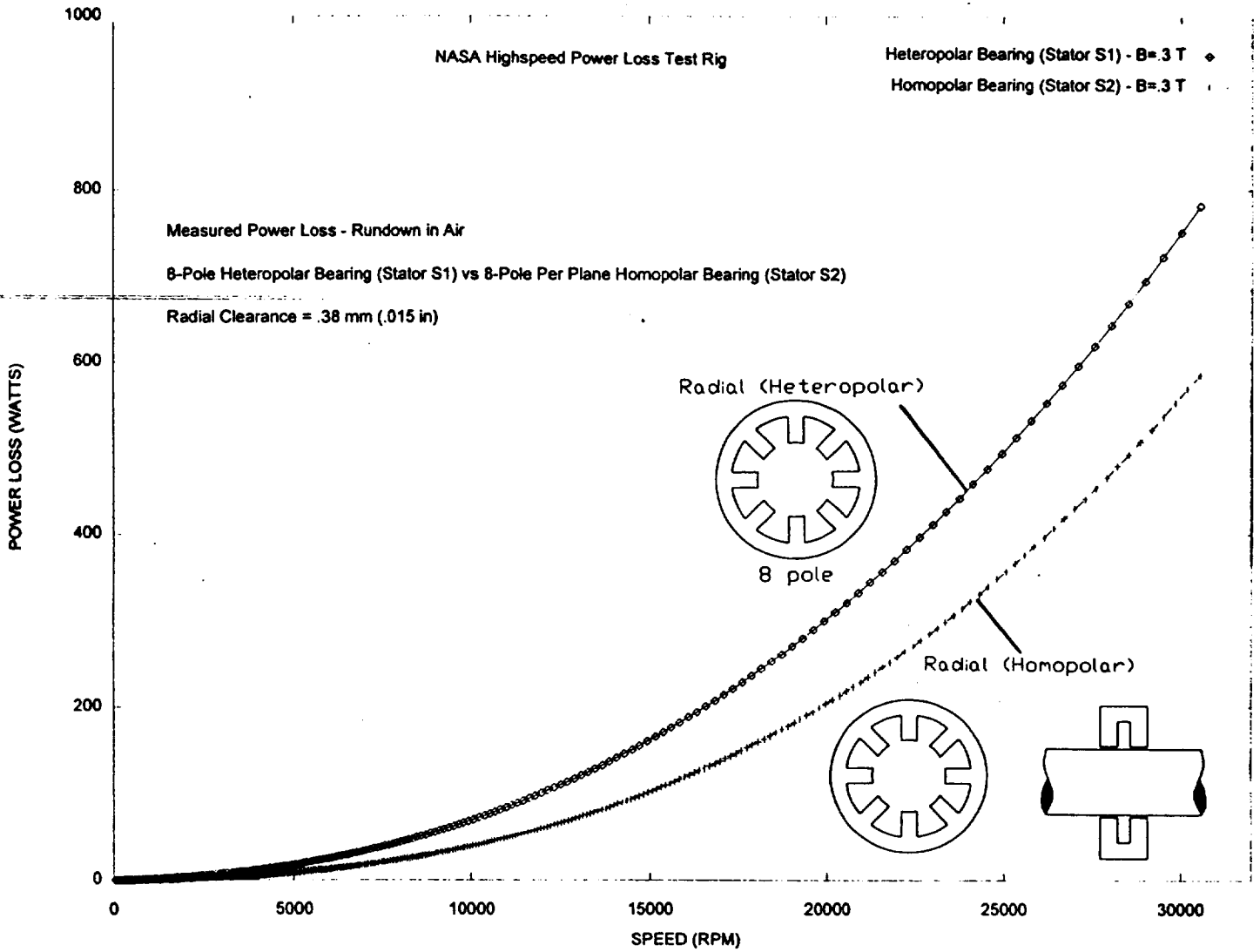Figure 2.6 Rundown Data for Homopolar vs. Heteropolar Bearing

Page 2.11

Figure 2.7 Power Loss Data for Homopolar vs. Heteropolar Bearing

Page 2.12

SECTION 3

FINITE ELEMENT MODELING

MAGNETIC VECTOR POTENTIAL FORMULATION

The equations for the magnetic field intensity and electric field intensity in a magnetic bearing are solved in a stator fixed coordinate system so they are not time dependent. Maxwell's equations for the magnetic flux density, B, the electric field, E, the magnetic field, H, and current density, J, are

$$\nabla \cdot \bar{B} = 0$$

$$\nabla \times \bar{H} = \bar{J} \qquad\qquad (1)$$

$$\nabla \times E = \nabla \times (\bar{U} \times \bar{B})$$

Here Faraday's law includes the rotor magnetic material moving with velocity U relative to the stator fixed coordinate system. The magnetic vector potential A is defined by the equation

$\bar{B} = \nabla \times \bar{A}$ which satisfies $\nabla \cdot \bar{B} = 0$.

The material relations are

$$\bar{J} = \sigma \bar{E} \quad and \quad \bar{H} = \nu \bar{B} \qquad\qquad (2)$$

with the magnetic reluctivity ν and the conductivity σ. Typically, with finite elements, the reluctivity is more convenient to use than the permeability.

In Ampere's law, the current density on the right hand side is split into a known coil current density, J_s, defined in the coil volume, and an unknown eddy current density, J_e defined in the remaining bearing analysis volume. Faraday's law can be written as the curl of a vector quantity which equals zero. Thus it can be expressed as the gradient of an electric scalar potential, ϕ. The expression can then be found:

$$\bar{J}_e = \sigma[-\nabla\phi + \bar{U}\times(\nabla\times\bar{A})] \qquad\qquad (3)$$

Ampere's law becomes

$$\nu \nabla X(\nabla X \bar{A}) + \sigma \nabla \phi - \sigma \bar{U} X(\nabla X \bar{A}) = \bar{J}_s \qquad (4)$$

Defining the gauge of Maxwell's equations as

$$\nu \nabla \cdot (\bar{A}) + \sigma \phi = 0 \qquad (5)$$

and using several vector identities, Ampere's law is transformed to

$$\nu \nabla \cdot \nabla \bar{A} + \sigma \bar{U} X(\nabla X \bar{A}) = - \bar{J}_s \qquad (6)$$

This is a suitable form for solution using finite elements.

TWO DIMENSIONAL FINITE ELEMENT FORMULATION

In two dimensions, the governing differential equation for the axial component of the magnetic vector potential, A_z, is obtained from the z component of (6) with the velocity terms included as

$$\nu \frac{\partial^2 A_z}{\partial x^2} + \nu \frac{\partial^2 A_z}{\partial y^2} - \sigma_z U_x \frac{\partial A_z}{\partial x} - \sigma_z U_y \frac{\partial A_z}{\partial y} + J_{sz} = 0 \qquad (7)$$

This equation applies to the case of a rotor with conductivity σ_z in the axial direction and can be used to model either a solid or laminated rotor. The magnetic vector potential equation is similar to the 2-D convection-diffusion equation in fluid mechanics. The rotor motion terms are evaluated using upwinding methods developed in the fluid mechanics area of research.

Let the finite element approximation to the solution be A*. The two dimensional differential equation becomes

$$\nu \frac{\partial^2 A_z^*}{\partial x^2} + \nu \frac{\partial^2 A_z^*}{\partial y^2} - \sigma_z U_x \frac{\partial A_z^*}{\partial x} - \sigma_z U_y \frac{\partial A_z^*}{\partial y} + J_{sz} = \epsilon_A(x,y) \qquad (8)$$

where $\epsilon_A(x,y)$ is the error [16]. The weighted residual for each element has the form

$$\{R_n^*\} = - \int_{A^*} \{W_n^*\} \, \epsilon_A^* \, dA^* \tag{9}$$

where A^e is the element area and n has the values 1,2,3,4 for a four node isoparametric element. The weighting functions are written as

$$\{W_{zn}\} = \{G_n\}^T + \frac{\beta_z \bar{h}_z}{2U_{mz}} [D_G]^T \{U_x\}^T \tag{10}$$

where G_n are the finite element shape functions, U_x are the rotor velocity components, and D_G is the matrix of the derivatives of the shape functions. The second term on the right provides the upwinding terms, adapted from computational fluids [19,20], necessary for the motion terms in the rotor. In this analysis, the upwinding term is only applied to the velocity terms, as is customary in finite elements for computational fluids.

The magnetic flux density must be evaluated from the magnetic vector potential. The magnetic flux density is given by

$$\begin{Bmatrix} B_x \\ B_y \end{Bmatrix} = \begin{bmatrix} 0 & 1 \\ -1 & 0 \end{bmatrix} \begin{Bmatrix} \dfrac{\partial A_z}{\partial x} \\ \dfrac{\partial A_z}{\partial y} \end{Bmatrix} \tag{11}$$

in two dimensions.

MAGNETIC BEARING APPLICATION

Magnetic field results have been obtained for the same bearings that were used in the power loss test rig of Section 2. The bearing has 8 poles, rotor OD = 90.9 mm (3.58 in), shaft OD = 50.8 mm (2.0 in), stator OD = 196.2 mm (7.726 in), axial length of bearing L = 43.6 mm (1.715 in) (without coils), and air gap = 0.762 mm (0.030 in). The radial length of each leg is 31.8 mm (1.253 in) and the circumferential width of each leg is 21.1 mm (0.79 in). The conductivity of the rotor is 1.03×10^7 1/Ωm in the axial direction and the relative permeability of the rotor and stator material is 3,000. Figure 3.1 shows the magnetic bearing geometry considered.

Figure 3.2 shows the finite element mesh. The mesh employed 4480 elements and 4640 nodes. Figure 3.3 shows the magnetic flux
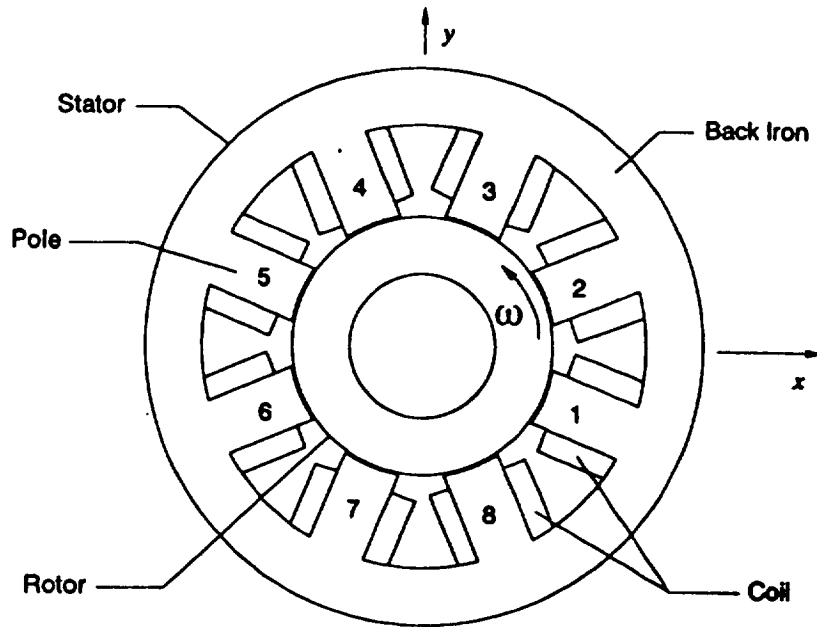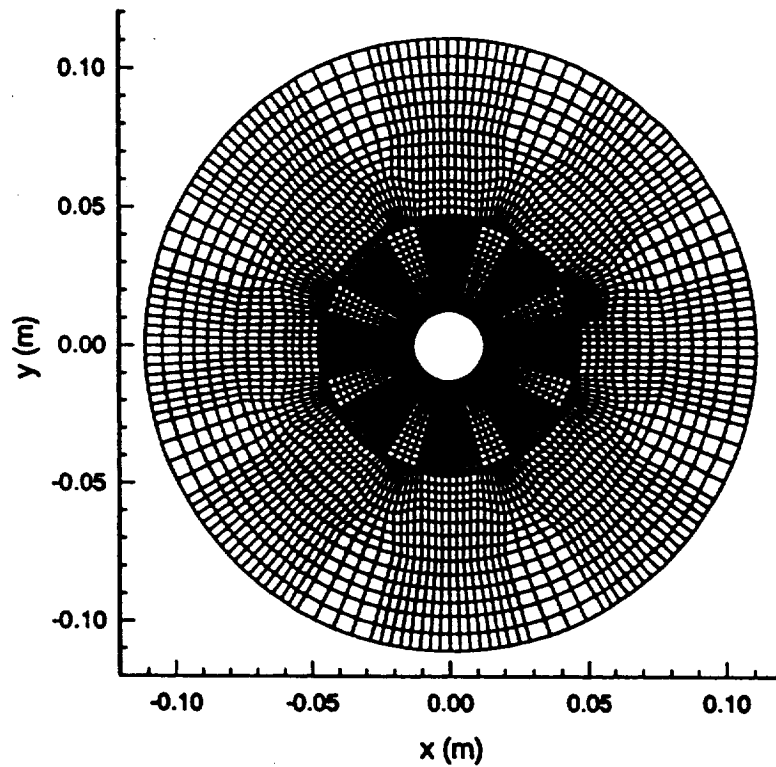
Figure 3.1. Magnetic Bearing Geometry

Figure 3.2. Finite Element Mesh

contours in the bearing at 0 rpm when all of the poles are activated with NI = 420 amp-turns. Figure 3.4 gives the calculated magnetic vector potential A_z plotted along the rotor surface at 0 rpm. The values calculated for upwinding on and upwinding off are identical, as expected.

Fig. 3.5 shows the magnetic vector potential at the rotor surface for a solid rotor at 955 rpm. Values for 95.5 rpm are given in [20]. The peak flux levels decrease slightly due to the rotation effects. Fig. 3.6 gives a plot of the magnetic vector potential at the rotor surface for a solid rotor at 9,550 rpm. The effects of rotor motion become quite significant for this high speed due to the opposing flux generated by the eddy currents generated in the rotor. Figs. 3.5 and 3.6 show curves with both upwinding on and upwinding off. The results are nearly identical showing that upwinding is not needed for a two dimensional analysis where a full 360 degree bearing model is evaluated.

Figure 3.7a shows the magnetic flux density plot for 0 rpm in a solid rotor and Fig. 3.7b gives the magnetic flux density plot for 95.5 rpm. For the static case, the maximum flux density occurs at the corners where the poles meet the back iron. At 95.5 rpm, the maximum flux density occurs in the rotor between the poles (this is much better seen in color contour plots than the black and white plots presented here). The flux density lines in the rotor are much closer to the rotor surface for the 95.5 case. In all cases, the magnetic flux density is the same for each pole so there is no net force generated.

Figure 3.7c gives the results for the rotor speed of 955 rpm while Fig. 3.7d shows the magnetic flux density plots for 9550 rpm. The stator contour lines at 955 rpm give a maximum value between the poles while at 9550 rpm the maximum occurs at the pole tips. The effect of upwinding is negligible in all cases. The peak values of flux are given in Table 3.1. It can easily be seen that the peak flux value and its location changes considerably in the bearing, at least for a solid rotor, due to rotor rotation effects. The predicted air gap flux increases with speed somewhat and then drops off rapidly as the flux generated by induced eddy currents becomes on the same order as the flux imposed by the coil currents.

The magnetic bearing forces were evaluated for this bearing using methods discussed in [20]. However, because all of the poles are operated at the same (bias) current levels, the force is zero.
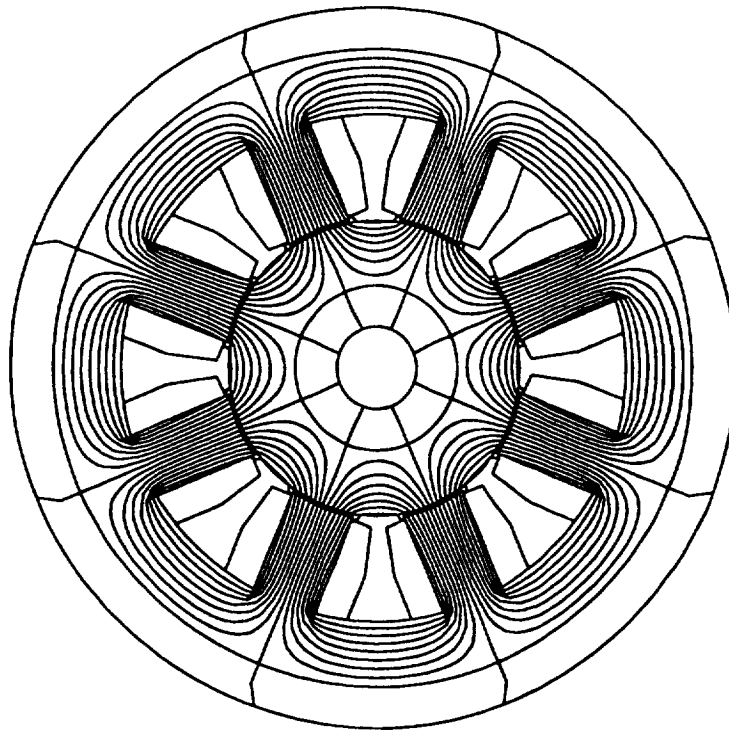
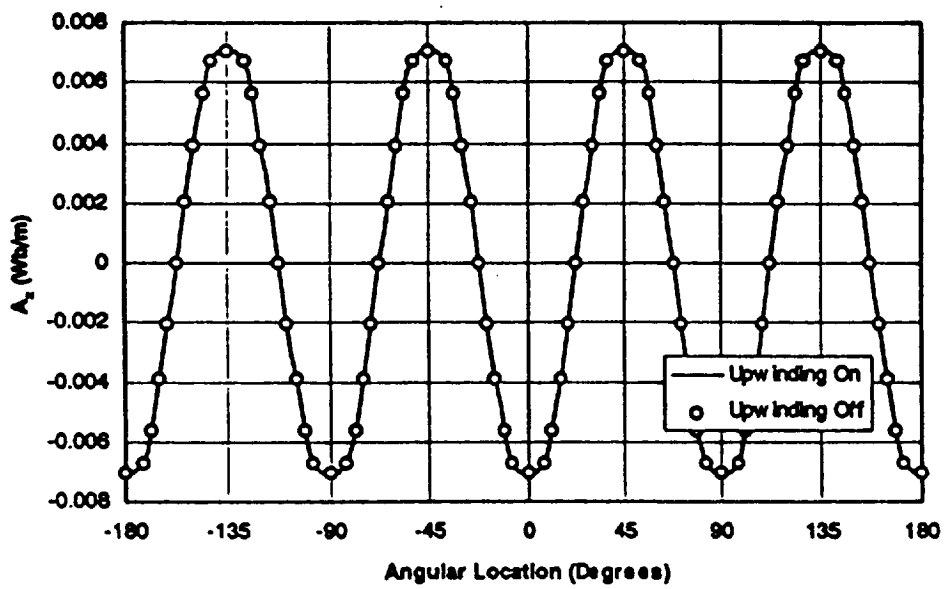Figure 3.3. Magnetic Flux Lines For 0 rpm

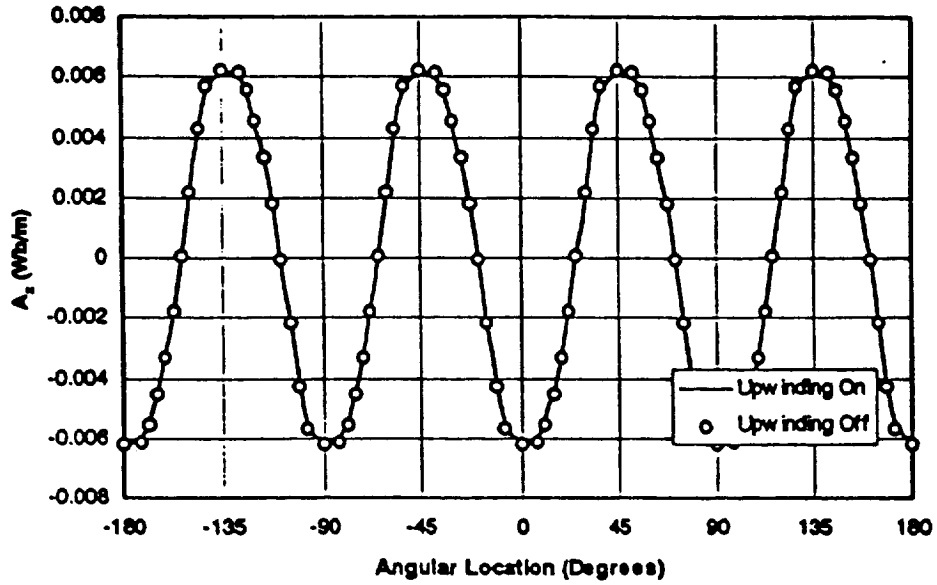Figure 3.4. Magnetic Vector Potential, A_z, At Rotor
Surface For 0 rpm

Page 3.6

Figure 3.5. Magnetic Vector Potential at Rotor Surface For 955 rpm For Solid Rotor
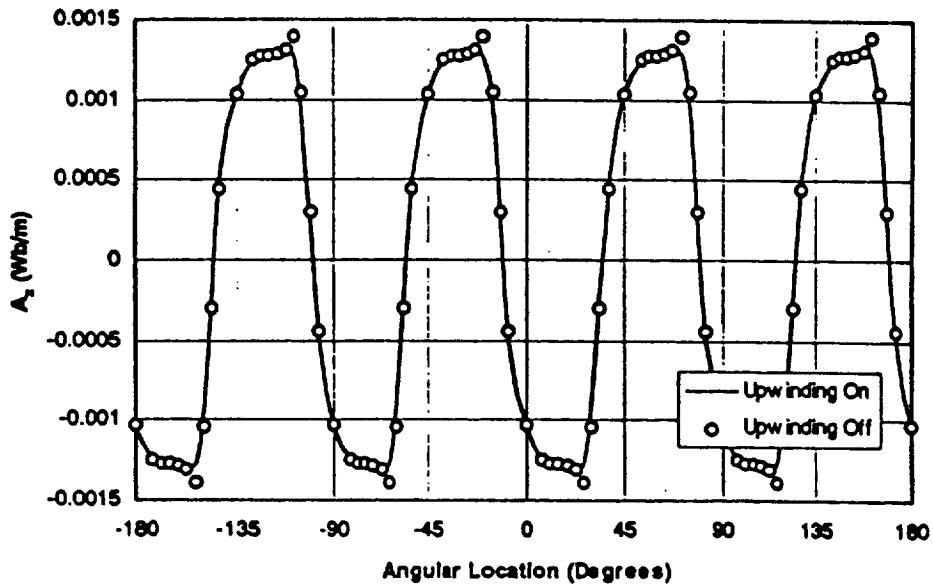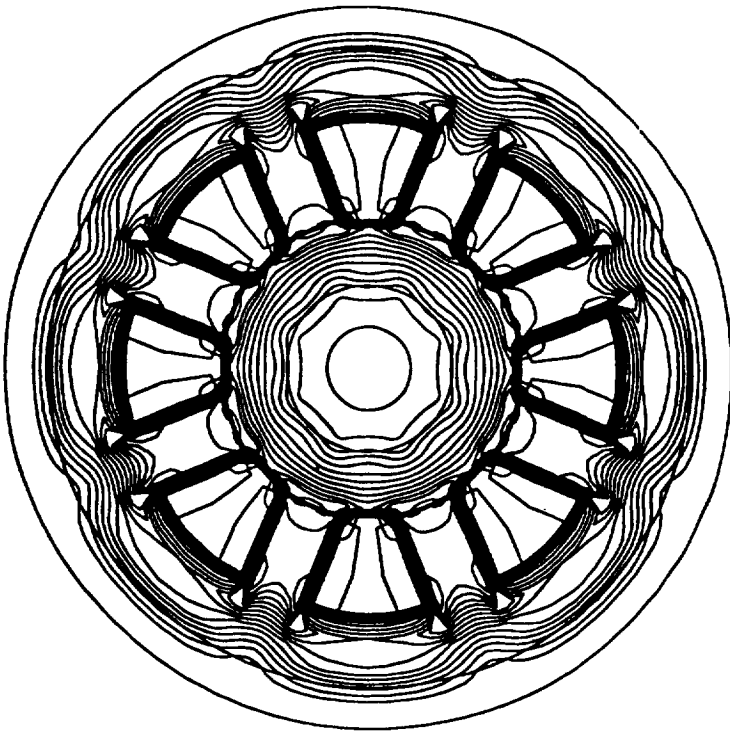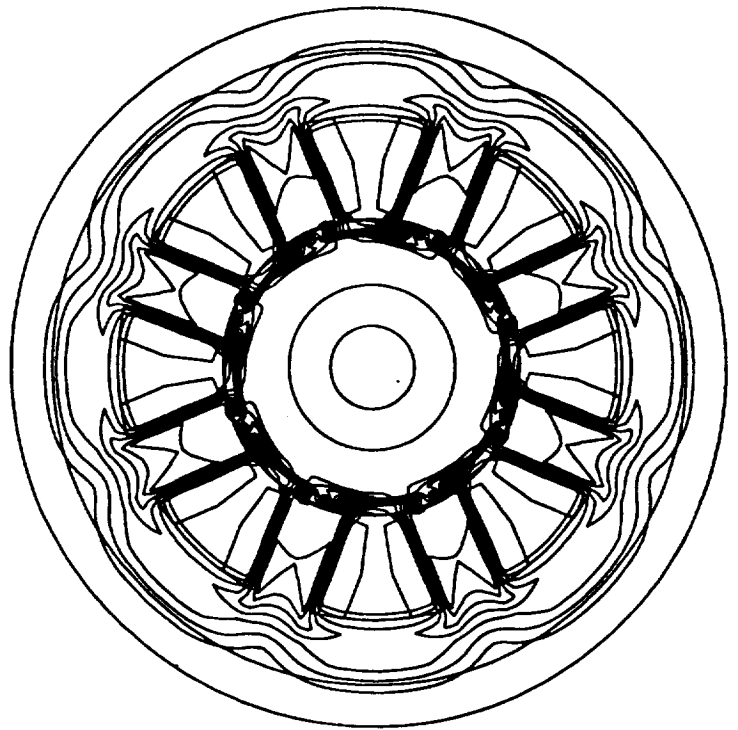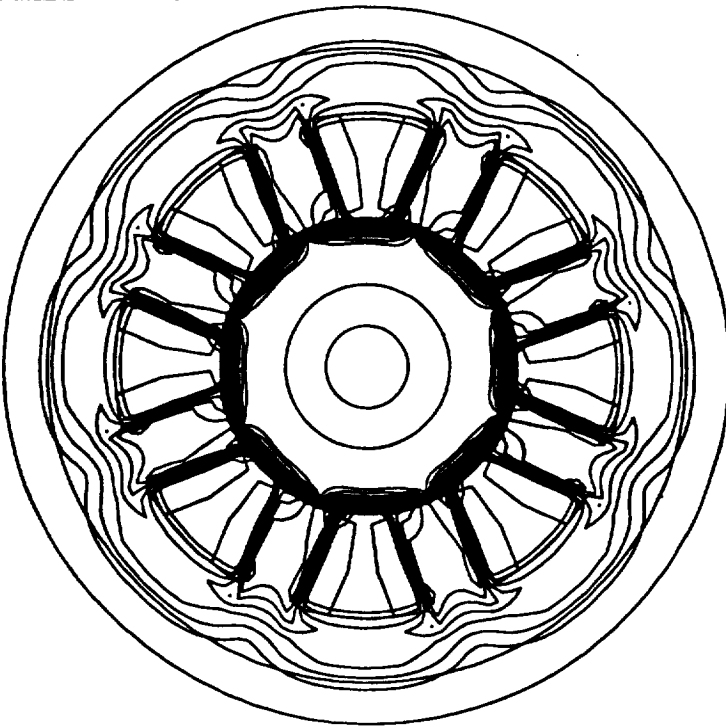

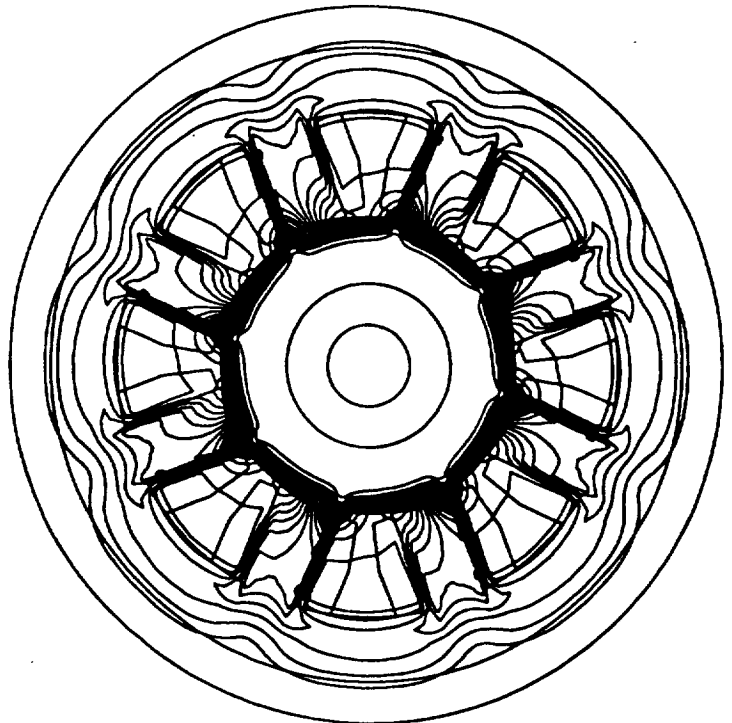**Figure 3.6.** Magnetic Vector Potential at Rotor Surface At 9550 rpm For Solid Rotor

Page 3.7

a) 0 rpm

b) 95.5 rpm

c) 995 rpm

d) 9550 rpm

Figure 3.7. Magnetic Flux Lines For Solid Rotor

Page 3.8

ELECTRIC FIELDS, EDDY CURRENTS AND POWER LOSS

The scalar electric potential is obtained from the gauge of Maxwell's equations

$$\phi = - \frac{1}{\sigma} \nu \nabla \cdot (\bar{A}) \qquad (12)$$

as shown in Rockwell [13]. The electric field intensity is given by

$$\bar{E} = - \nabla \phi + \bar{U} \times (\nabla \times \bar{A}) \qquad (13)$$

The current densities in the bearing are determined from

$$\bar{J} = \sigma[- \nabla \phi + \bar{U} \times (\nabla \times \bar{A})] \qquad (14)$$

where $\bar{J} = \sigma \bar{E}$. However, the current densities are divided into the known applied current densities in the coils and the motionally induced eddy currents in the rotor.

$$\bar{J} = \left\{ \begin{array}{ll} \bar{J}_s & , \ In \ Stator \\ \bar{J}_e & , \ In \ Rotor \end{array} \right\} \qquad (15)$$

The induced eddy current expression is then

$$\bar{J}_e = \sigma \left[-\nabla \phi + \bar{U} \times (\nabla \times \bar{A}) \right] \ , \ In \ Rotor \qquad (16)$$

in the rotor.

The power dissipation in the conductive material of the rotor is given by

$$P = \iiint_V (\bar{E} \cdot \bar{J}) \ dV \qquad (17)$$

where V is the volume of the rotor [14]. Using the material

relation, this becomes

$$P = \iiint_V (\frac{1}{\sigma} \bar{J} \cdot \bar{J}) \, dV \qquad (18)$$

It can be shown that the scalar electric potential is zero in the two dimensional case [9]. The eddy currents in the rotor are evaluated from

$$J_{z\bullet} = \sigma_z U_x \frac{\partial A_z}{\partial x} + \sigma_z U_y \frac{\partial A_z}{\partial y} \qquad (19)$$

The eddy currents have only an axial component. In two dimensions, the power loss expression becomes

$$P = \iint_A (\frac{1}{\sigma_z} J_z^2) \, dA \qquad (20)$$

for the magnetic bearing configuration considered in this paper.

MAGNETIC BEARING APPLICATION

The eddy currents and power losses in the rotor, for both solid and laminated rotors, have been obtained for the same bearing just discussed in the magnetic field evaluation. The conductivity of the rotor is 1.03×10^7 $1/\Omega m$ in the axial direction and the relative permeability of the rotor and stator material is 3,000.
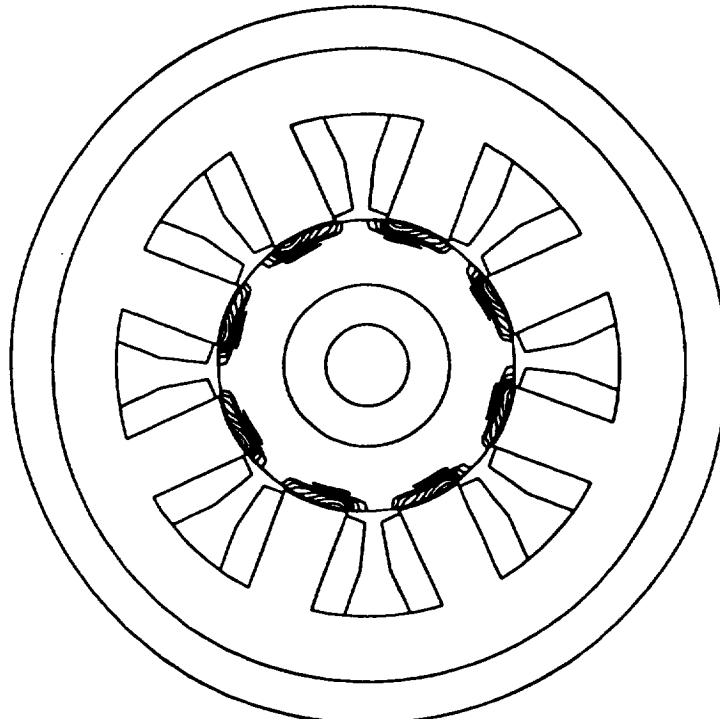
EDDY CURRENTS IN SOLID ROTOR

The eddy currents were calculated using a full 360 degree, two dimensional model of the bearing. All poles were activated with equal values of NI. The induced eddy current contours were calculated and plotted to illustrate the rotational effects without laminations. Upwinding was employed for these calculations although the results did not exhibit significant numerical instabilities. Of course, there are no eddy currents for the case of zero shaft rotation.

Figure 3.8 shows the eddy current patterns in the rotor for 95.5 rpm. The eddy currents are shown as being generated relatively near the surface of the rotor and shifted in the direction of the shaft motion. This effect is shown more clearly in Rockwell et al. [8] where only two poles were activated.
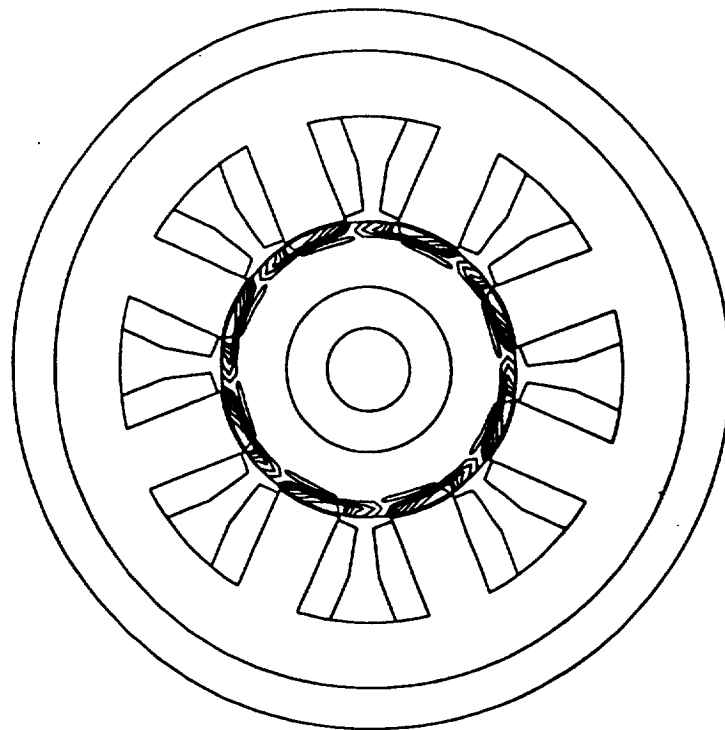
Figure 3.8. Eddy Current Density in Magnetic Bearing
With Solid Rotor at 95.5 rpm

Figure 3.9. Eddy Current Density in Magnetic Bearing
With Solid Rotor at 955 rpm

Page 3.11

Figure 3.9 shows the results for 955 rpm. The eddy currents are closer to the rotor surface than in the 95.5 rpm case. Figure 3.10 shows the induced eddy currents in the solid rotor for 9550 rpm. The eddy currents appear in the rotor under the trailing edges of the poles but not under leading edges of the poles.

Matsumura [2] and Kasarda et al. [4] discussed the possibility that the eddy currents develop under both the leading and trailing edges of the poles. However, the calculated results in this paper indicate that the eddy currents due to shaft rotation develop in the rotor only under the trailing edge of the poles.

The power loss for the solid rotor is shown in Fig. 3.11. It increases substantially up to a peak value and then levels off at the maximum value. At high speed, all of the coil energy goes into producing eddy currents, with the resulting induced flux opposing the air gap flux. No net air gap flux is generated at high speeds.

LAMINATION EFFECTS

Industrial magnetic bearings are not constructed with solid rotors because high eddy currents are produced. These negatively impact the performance of the bearing. The rotor magnetic material is laminated with thin radial (pancake) laminations to reduce eddy currents. These laminations are electrically separated by a thin layer of insulation and glue which severely restricts the axial conductivity of the rotor materials. Thus, the eddy currents cannot establish themselves in the axial direction. The approach employed in this work is to use an effective axial conductivity for the magnetic material to model the effect of the laminations.

Experimental results on power losses in magnetic bearings indicate that the eddy current losses are proportional to the rotor speed squared, $P \propto \omega^2$ [3,4,11,12]. The power loss equation is given by

$$P = \iint_A (\frac{1}{\sigma_z} J_z^2) \, dA \tag{21}$$

where the integral is evaluated over the rotor area. As the rotational frequency increases, the eddy currents occupy a smaller and smaller area of the rotor, so the area is assumed to be approximately inversely proportional to the rotor speed, $A \propto 1/\omega$ as is typical of eddy currents as indicated by Stoll [15]. The power loss formula employed here is thus assumed to be linearly proportional to the conductivity and speed, or $P \propto \sigma_z \omega$.
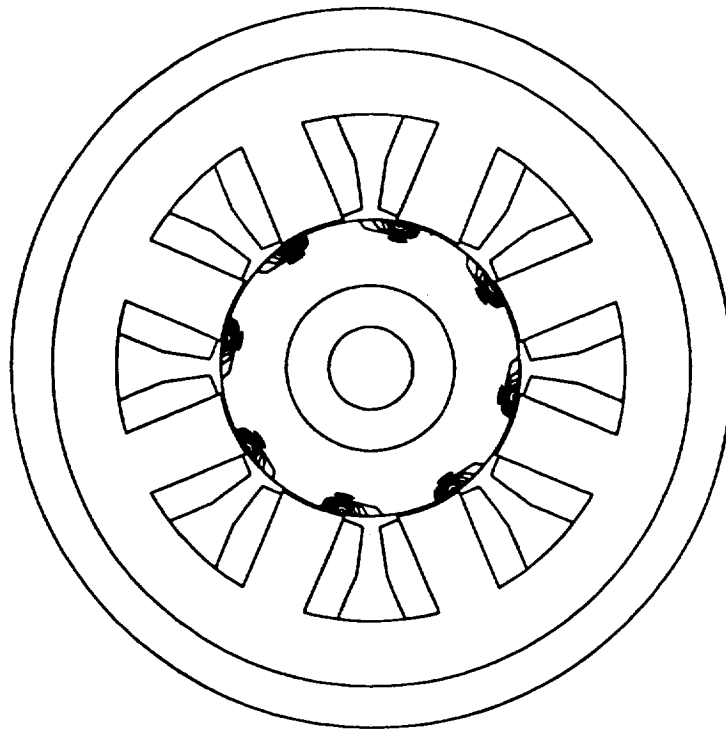
Figure 3.10. Eddy Current Density in Magnetic Bearing
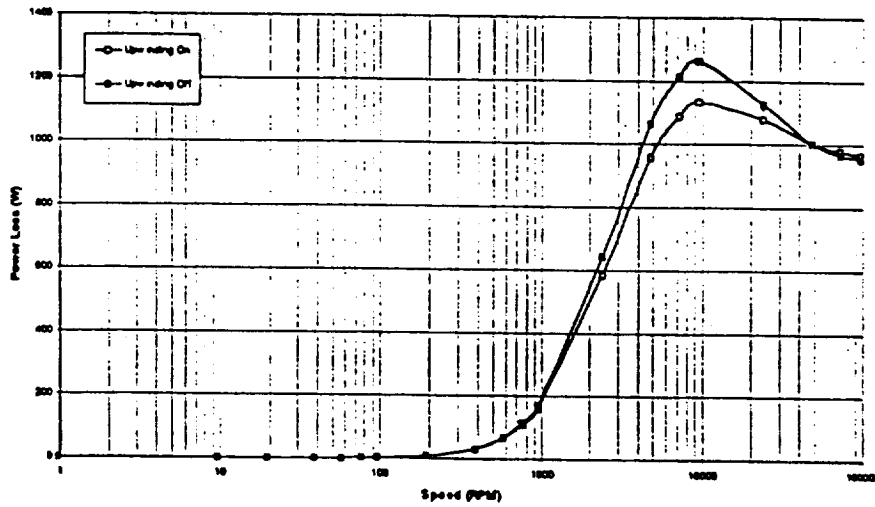With Solid Rotor at 9550 rpm

Figure 3.11. Rotor Eddy Current Power Loss vs. Rotor Speed
For Solid Rotor Model

Page 3.13

The effective conductivity is therefore chosen to be proportional to the angular velocity of the rotor, $\sigma_{z,eff} \propto \omega$.

COMPARISON TO EXPERIMENTAL POWER LOSSES

Kasarda et al. [3] discussed the design of the present high speed test rig in some detail and gave a sensitivity analysis of the loss modeling based upon the theoretical parameters involved. Kasarda et al. [4] presented high speed loss results, using the same test rig, for an 8 pole radial bearing constructed of silicon iron laminated materials. The rotor operated at a top speed of about 32,000 rpm, corresponding to a DN value of 2.9×10^6 mm rpm. An analytical /empirical model was then applied to the loss measurements by Kasarda et al. [12] to separate the loss into eddy current, hysteresis, and windage effects.

The experimental power loss measurements for the bearing considered here were presented in Allaire et al. [13]. The eddy current losses have been evaluated and the results plotted in Figs. 3.12 and 3.13. The finite element calculated values are also given in Figs. 3.12 and 3.13. The effective value of conductivity was $\sigma=5\omega$ where ω is in rad/sec. The agreement is excellent for the entire speed range as well as different values of air gap magnetic flux density and air gap thickness.
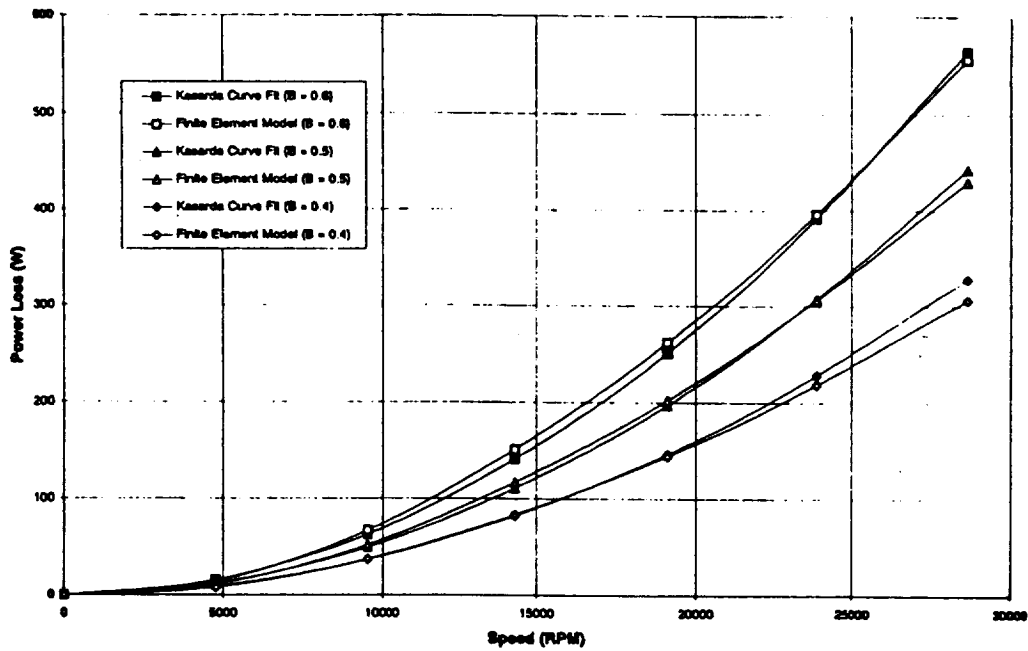
Figure 3.12. Rotor Eddy Current Power Loss vs. Rotor Speed
For Laminated Rotor at Air Gap of 0.76 mm
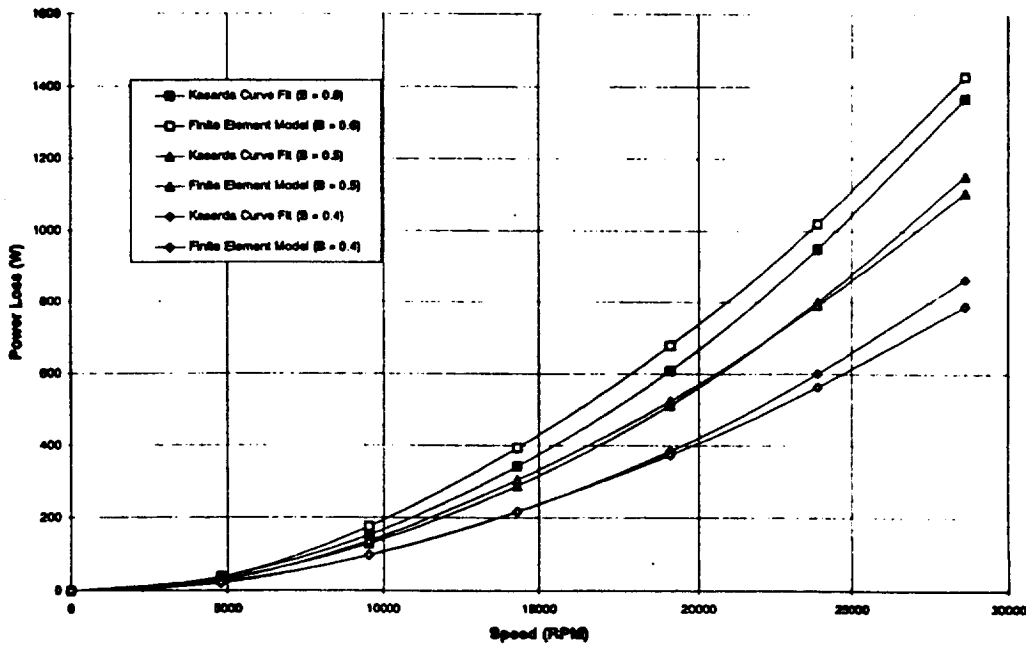- Comparison of Finite Element vs. Experimental Results

Figure 3.13. Rotor Eddy Current Power Loss vs. Rotor Speed
For Laminated Rotor at Air Gap of 0.38 mm
- Comparison of Finite Element vs. Experimental Results

Page 3.15

REFERENCES

1. Matsumura, F., Fujita, M., and Ozaki, Y., 1988, "Characteristics of Friction on Magnetic Bearings," Trans. IEE of Japan, 108-D, No. 5, pp 462-468.

2. Higuchi, T., Mizuno, T., and Miyake, S., 1986, "Experimental Study of Rotational Loss in Magnetic Bearings," Proc. Conf. IPE, Japan, pp. 53-54.

3. Ueyama, H., and Fujimoto, Y., 1990, "Iron Losses and Windy Losses of Rotational Speed Rotor Suspended by Magnetic Bearings," Proceedings of 2nd International Symposium on Magnetic Bearings, Tokyo, Japan, pp. 237-242.

4. Matsumura, F., and Hatake, K., 1992, "Relation between Magnetic Pole Arrangement and Magnetic Loss in Magnetic Bearing," Proceedings of Third International Conference on Magnetic Bearings, Alexandria, Virginia, USA, pp. 274-283.

5. Kasarda, M.E., Allaire, P.E., Hope, R.W., and Humphris, R.R., 1993, "Measured and Predicted Losses in Planar Radial Magnetic Bearings," Proceedings of Mag '93, Alexandria, VA.

6. Kasarda, M.E., and Allaire, P.E., 1995, "Experimentally Measured and Improved Calculated Losses in Planar Radial Magnetic Bearings," Accepted for STLE Transactions, 1996.

7. Kasarda, M. E. F., Allaire, P. E., Maslen, E. H. and Gillies, G. T., 1994, "Design of a High Speed Rotating Loss Test Rig For Radial Magnetic Bearings," Proceedings, Fourth International Symposium on Magnetic Bearings, ETH Zurich.

8. Kasarda, M. E. F., Allaire, P. E., Maslen, E. H., Brown, G. R., and Gillies, G. T., "High Speed Rotor Losses in a Radial 8-Pole Magnetic Bearing, Part 1: Experimental Measurement," Paper 96-GT-470, International Gas Turbine Conference, Birmingham, England, June 1996.

9. Kasarda, M. E. F., Allaire, P. E., Maslen, E. H., Brown, G. R., and Gillies, G. T., "High Speed Rotor Losses in a Radial 8-Pole Magnetic Bearing, Part 2: Analytical/Empirical Models and Calculation," Paper 96-GT-471, International Gas Turbine Conference, Birmingham, England, June 1996.

10. Allaire, P. E., Kasarda, M. E. F., Maslen, E. H., and Gillies, G. T., "Rotor Power Loss Measurements for Heteropolar and Homopolar Magnetic Bearings," Fifth International Conference on Magnetic Bearings, Kanazawa, Japan, August 28-30, 1996, pp. 271-276.

11. Sarma, M. S., "Potential Functions in Electromagnetic Field Problems," IEEE Trans. on Magnetics, Vol. MAG-6, No. 3,

September, 1970, pp. 513-518.

12. Muramatsu, K., Nakata, T., Takahashi, N., and Fujiwara, K., "Comparison of Coordinate Systems for Eddy Current Analysis in Moving Conductors," IEEE Trans. on Magnetics, Vol 28., No. 2, 1992, pp. 1186-1189.

13. Chan, E. K. C., and Williamson, S., "Factors Influencing the Need for Upwinding in Two Dimensional Field Calculations," IEEE Trans. on Magnetics, Vol. 28, No. 2, 1992, pp. 1611-1614.

14. Ito, M., Takahashi, T., and Odamura, M., "Up-Wind Finite Element Solution of Traveling Magnetic Field Problem," IEEE Trans. on Magnetics, Vol. 28, No. 2, 1992, pp. 1605-1610.

15. Allaire, P. E., Rockwell, R. D., and Kasarda, M. E. F., "Magnetic and Electric Field Equations for Magnetic Bearing Applications", Transactions of MAG '95, Technomics Publishing, 1995, pp. 259-272.

16. Allaire, P. E., Basics of the Finite Element Method, W. C. Brown (distributed by West Publishing), 1985.

17. Hughes, T. J. R., "A Simple Scheme for Developing 'Upwind' Finite Elements," International Journal for Numerical Methods in Engineering, Vol. 12, No. 9, 1978, p. 1359.

18. Hahn, S., Bigeon, J., and Sabonnadiere, J., "An 'Upwind' Finite Element Method for Electromagnetic Field Problems in Moving Media," International Journal for Numerical Methods in Engineering, Vol. 24, No. 11, 1987, p. 2071.

19. Heinrich, J. C., and Yu, C. C., 1988, "Finite Element Simulations of Buoyancy-Driven Flows with Emphasis on Natural Convection in a Horizontal Circular Cylinder," Computational Methods of Applied Mechanics in Engineering, Vol. 69, pp. 1-27.

20. Pepper, D. W. and Henrich, J. C., The Finite Element Method: Basic Concepts and Applications, Hemisphere Publishing, 1992.

21. Rockwell, R. D., Allaire, P. E., Heinrich, J. C., and Foshage, G. K., "Magnetic Field Finite Element Modeling of Magnetic Bearings Including Rotor Motion Effects and Eddy Currents," 5th International Symposium on Magnetic Bearings, Kanazawa, Japan, August, 1995, pp. 241-246.

22. Rockwell, R. D., "2D Electromagnetic Finite Element Modeling of Magnetic Bearings Including Rotation Effects," M. S. Thesis, University of Virgina, 1996.

23. Rockwell, R. D., Allaire, P. E., and Kasarda, M. E. F., "Radial Planar Magnetic Bearing Analysis with Finite Elements – Part 1: Magnetic Fields," Submitted to ASME Turbo Expo, Orlando, June 1997.

24. Allaire, P. E., Rockwell, R. D., and Kasarda, M. E. F., "Radial Planar Magnetic Bearing Analysis with Finite Elements - Part 2: Eddy Currents and Rotor Power Losses," Submitted to ASME Turbo Expo, Orlando, June 1997.

DISTRIBUTION LIST

1 - 3	National Aeronautics and Space Administration Lewis Research Center Mail Stop 500-309 21000 Brookpark Road Cleveland, OH 44135 216-433-2457 Attention: Ms. Kaprice Harris, Grants Officer
4	Mr. Andrew Provenza, Project Monitor National Aeronautics and Space Administration Lewis Research Center Mail Stop 23-3 21000 Brookpark Road Cleveland, OH 44135 216-433-6047
5 - 6	P. E. Allaire
7	R. D. Flack, Jr.
8 - 9	M. Rodeffer, Clark Hall
10	J. Duckett, Jr., Contract Analyst Armstrong Data Services, Inc. 2707 Chain Bridge Road Suite 150 Vienna, VA 22182 703-827-2347
11 - 12	NASA Scientific and Technical Information Facility P. O. Box 8757 Baltimore/Washington International Airport Baltimore, MD 21240
*	SEAS Postaward Research Administration
13	SEAS Preaward Research Administration

JO#7449:ph